Porous pyroelectric ceramic with carbon nanotubes for high-performance thermal to electrical energy conversion

Qingping Wang[a, b+], Shihua He[c+], Chris R Bowen[b*], Xiao Xiao[d], Jin An Sam Oh[e], Jianguo Sun[f], Kaiyang Zeng[c], Wen Lei[g, h*], Jun Chen[d*]

[a] Department of Physics & Mechanical and Electronic Engineering, Hubei University of Education, Wuhan 430205, P. R. China
[b] Department of Mechanical Engineering, University of Bath, Claverton Down Road, Bath BA2 7AY, UK
[c] Department of Mechanical Engineering, National University of Singapore, 9 Engineering Drive 1, 117576, Singapore
[d] Department of Bioengineering, University of California, Los Angeles, Los Angeles, CA 90095, USA
[e] Singapore Institute of Manufacturing Technology, Agency for Science, Technology and Research (A*STAR), 2 Fusionopolis Way, Innovis, 138634 Singapore
[f] Department of Materials Science and Engineering, National University of Singapore, Singapore 117574, Singapore
[g] School of Optical and Electronic Information, Key lab of Functional Materials of Electronic Information (B) of MOE, Huazhong University of Science and Technology, Wuhan 430074, P. R. China
[h] Wenzhou Advanced Manufacturing Institute, Huazhong University of Science and Technology, Wenzhou, 325035, P. R. China
[+] These authors contributed equally to this work.
Email addresses: wenlei@mail.hust.edu.cn(W.L.); jun.chen@ucla.edu(J.C.); msscrb@bath.ac.uk(C.B.)

Abstract: The recycling of low-grade thermal energy from our surroundings is an environmental-friendly approach to contribute to sustainability, which remains a grand challenge. Herein, a high-performance porous pyroelectric ceramic formed using carbon nanotubes (CNT) is designed and fabricated using a modified solid-state reaction technique. Localised characterization of PMN-PMS-PZT and PMN-PMS-PZT with 0.3 wt.% CNT additions by piezoelectric force microscopy suggests that the presence of porosity and defects in grains can restrict the reversal of domains and weaken the local piezoresponse; this is due to the influence of porosity on the electric field, domain morphology, or screening effects induced by defects at the pore surface. More importantly, the porous ceramics showed enhanced figure of merits, including voltage responsibility and energy harvesting figure of merit, compared to the dense ceramic. The harvested energy increased by 208% when the 0.3 wt.% of CNT was added to produce porosity, which has a potential application in thermal energy harvesting and sensing system.

Key words: Pyroelectricity; Porous pyroelectric ceramic; PFM; CNT; FOMs; Thermal energy harvesting

1. Introduction

With global increasing energy consumption, the shortage of natural energy resources [1, 2], and the growth on the Internet of Things (IoT) [3-6], the development of new materials for energy harvesting and sensing is a topic of intense interest in the quest to produce autonomous, battery-free and self-powered system [7-11]. Among them, pyroelectric energy harvesting technology uses energy conversion between thermal energy and electrical energy to provide an environmental-friendly form of power from waste heat. This is achieved through alternatively heating and cooling pyroelectric materials to modulate the level of polarization and thereby produce charge [1, 12-14]. The efficiency of the conversion of a temperature change to an electrical charge, voltage or energy for sensing and harvesting is often determined by appropriate figure of merits (FOMs) for a given pyroelectric material. These FOMs can be expressed by the,

current responsivity,

$$F_I = p/C_E \tag{1}$$

voltage responsivity,

$$F_V = p/\varepsilon_r\varepsilon_0 C_E \tag{2}$$

detection figure of merit,

$$F_D = p/C_E(\varepsilon_r\varepsilon_0 \tan\delta)^{0.5} \tag{3}$$

and *energy harvesting figure of merit*,

$$F_E^{'} = p^2/\varepsilon_r\varepsilon_0 C_E^2 \tag{4}$$

where p is the pyroelectric coefficient, ε_r and ε_0 are the relative permittivity and permittivity of free space, respectively, $\tan\delta$ is the dielectric loss tangent, and C_E is the volume specific heat capacity [12, 15].

Since the pyroelectric coefficient, dielectric properties and heat capacity are often interconnected, attempts to improve a specific figure of merit by changing a single parameter provides a challenge to improve the overall performance of pyroelectric energy harvester. Several strategies have been developed for improving the harvesting figures of merit. For example, optimizing the pyroelectric coefficient can be accomplished by chemical modification [16-18], microstructural design [19-21], using novel experimental techniques, and applying a direct current bias field [22, 23]. Reducing the permittivity and volume specific heat capacity, can be achieved by introducing porosity in the microstructure of the materials [24]. Finally, entirely new materials

[25] and structural design [26-28] approaches have been developed to improve the pyroelectric performance. Nevertheless, the concept of pyroelectric energy harvesting continues to suffer from a small power output and poor conversion efficiency, thereby limiting the potential practical application. Therefore, the performance requires a further improvement to enhance the relevant figures of merit (FOMs). It has been reported that porous structures fabricated from pyroelectric ceramics have higher pyroelectric FOMs compared to a dense material since porosity acts to decrease both the permittivity and volume heat capacity [29]; see Equations 1 to 4. However, the introduction of porosity also decreases the pyroelectric coefficient, p, and a performance benefit will only be achieved if the pyroelectric coefficient is not reduced significantly, in particular due to the p^2 dependence of F_E' (Equation 4). This complex relationship between the thermal and dielectric properties means that there is potential to tune the porosity to achieve the optimum pyroelectric response of energy harvesters and sensors.

Among the various strategies for producing porous materials [15, 22, 30-33], a simple and low-cost method is to use a volatile pore-forming agent (PFA) that is added to the ceramic prior to powder compaction, which is then burned out during the high temperature sintering process. A variety of pore formers such as poly(methyl methacrylate) (PMMA) [34], poly(vinyl alcohol) (PVA) [35], poly(ethylene oxide) (PEO) [36], dextrin and self-raising flour [29], have been proposed to enhance the performance of ceramics through tailoring the pore size and morphology in a variety structures. However, defects and cracks are often introduced into the ceramic between due to volatile gases produced during burn out of the pore forming agent, which can reduce the pyroelectric and mechanical properties. Therefore, careful selection of both the pore forming agent and the appropriate thermal treatment is required to achieve the desired structure. To solve the above problems, carbon nanotubes (CNT) as a fine-scale pore former was chosen to improve the pyroelectric coefficient and figures of merit in this work.

This work demonstrates that the presence of porosity and defects can influence domain reversal and local piezoresponse due to the electric field distribution within the porous material. In addition, the permittivity and specific heat capacity was decreased by the introduction of the pore forming nanotubes, while the pyroelectric figures of merit and output voltage of pyroelectric energy harvesters were dramatically improved. This work therefore demonstrates the potential of this new approach in applications related to low-power electronics devices and wireless sensor networks.

2. Experimental Section

2.1. Preparation of porous ceramics PMN-PMS-PZT: *x*CNT

Pyroelectric ceramics of $Pb[(Mn_{1/3}Nb_{2/3})_{1/2}(Mn_{1/3}Sb_{2/3})_{1/2}]_{0.04}(Zr_{0.95}Ti_{0.05})_{0.96}O_3$: *x*CNT (PMN-PMS-PZT: *x*CNT, where *x* is the weight ratio of CNT added to PMN-PMS-PZT and *x* = 0, 0.3, 0.6, 0.9, and 1.2) were fabricated by a modified solid-state reaction technique. The raw materials were PbO (99%), ZrO_2 (99.9%), TiO_2 (99.8%), Nb_2O_5 (99.5%), Sb_2O_3 (99%), CNT (50%), $Mn(NO_3)$ (50%) and deionized water were used as solvents. A 10 mol% excess of PbO was introduced to compensate for the lead loss during the following high temperature sintering and prevent the formation of the pyrochlore phase in the ceramics. Subsequently, all disk samples were prepared along with the conventional procedure and sintered at 1230 °C for 2 – 4 h in air [37] and were poled under a *dc* field of 3.0 – 4.0 kV mm^{-1} at 30 °C in a silicone oil bath. Top and bottom electrodes of the ceramics were prepared by screen printing with silver paste for subsequent use.

2.2. Characterization

The microstructures of the samples were analyzed by X-ray diffraction (X'Pert-PRO, PANalytical B.V.) and field-emission scanning electron microscopy (FE-SEM Sirion 200, FEI), respectively. The dielectric constant (relative permittivity) and loss tangent as a function of temperature were measured with an impedance analyzer (Agilent4294A, Agilent Technology Inc., Santa Clara, CA). The polarization-electric field (*P-E*) hysteresis loops were measured using a ferroelectric test system (CPE1601, PolyK Technologies, USA). The pyroelectric coefficient was determined by the Byer-Roundy method and derived from the equation as $p = I/A \times (dT/dt)$, where I is the pyroelectric current, A is the effective electrode area, and dT/dt is the rate of temperature change, respectively. The pyroelectric current was measured using an electrometer (Picoammeter 6485, Keithley Instruments, Cleveland, OH). The specific heat capacity C_p was evaluated according to the equation:

$$C_p = C_{p(dense)}(1-\varphi) \tag{5}$$

where φ denotes the porosity fraction and $C_{p\ (dense)} = 0.29$ J g^{-1} K^{-1} was observed through a diffraction scanning calorimeter (DSC8000, Perkin Elmer, USA). The bulk density of the samples (ρ) was measured by the Archimedes method and the volume heat capacity (C_v) was calculated though $C_v = \rho C_p$.

For characterization by piezo-force microscopy (PFM), the samples were firstly ground and then polished

using diamond spray polishing compounds with particle size of 1, 0.5 and 0.2 μm for 3 h, respectively. Pt/Ir -coated conductive tips (Nanosensor, PPP-NCLPt, Switzerland) were used for all PFM measurements that was based on atomic force microscopy (MFP-3D, Asylum Research, Oxford Instruments, Santa Barbara, CA, USA) equipped with high voltage and high temperature modules. Local piezoresponse hysteresis loops were measured using switching spectroscopy piezoresponse force microscopy (SS-PFM). Samples for transmission electron microscopy (TEM) observation included samples to assess the morphology, selected area electron diffractions (SAED), convergent beam electron diffraction (CBED) patterns, and scanning transmission electron microscopy images (STEM) were revealed by FEI Titan 80-300 electron microscopes with the accelerating voltage of 200 kV. The CBED patterns were acquired with a convergence half-angle of 2.5 mrad at room temperature on the same grain. The temperature and rate of temperature fluctuation was achieved using thermocouples and Peltier cells, respectively. The output voltage, current and power were obtained via a data acquisition system, which have been described in detail in our previous publication [38].

3. Results and Discussion

3.1. Morphology and PFM analysis of porous ceramic PMN-PMS-PZT: *x*CNT

3.1.1 Morphology

Fig. 1 shows a schematic of the synthesis process to produce the porous PMN-PMS-PZT: *x*CNT ceramics. The surface morphology and cross section morphology of the porous PMN-PMS-PZT ceramics formed using CNTs (see Fig. S1) at a range of contents are shown in Fig. S2 and Fig. S3, respectively. As can be seen from Fig. S2a and S3a, the surface and cross section of the pristine (CNT-free) PMN-PMS-PZT exhibited a dense, fine grained, and uniform microstructure, with no obvious porosity and a clear grain structure. With the addition of CNT as the pore former, pores with a range of sizes and morphologies appeared, as seen in Figs. S2b-e and S3b-e. As expected, increasing the CNT content led to the generation of a greater degree of porosity. It is of interest to note that some of the pores that are formed are relatively large, with a maximum length of ~ 2.16 μm, and this can be attributed to the partial agglomeration of CNT. In addition, as can be seen from Fig. S3, the number of pores and defects located in grains and at grain boundaries increased with an increase of CNT content.

3.1.2 Heat capacity

The mean density of the ceramics, obtained according to Archimedes' method, in Fig. S4a, decreases with increasing CNT content, since the CNTs are removed during the high temperature sintering process to produce pores. In addition, the porosity of the ceramics can be obtained according to the following equation (6):

$$Porosity = \left(1 - \frac{\rho_{porous}}{\rho_{dense}}\right) \times 100\% \quad (6)$$

Where ρ_{porous} and ρ_{dense} are the densities of the porous ceramic and the theoretical density of the ceramic, respectively. In this case, the porosity of the pristine PMN-PMS-PZT was assumed to approximately 0% porosity. With an increase of the CNT content, the porosity volume fraction increased from 2 vol.% to 8 vol.%; see Fig. S4b. The volume heat capacity of the ceramics can be derived from [39]

$$C_v = C_{v(dense)}(1 - porosity) \quad (7)$$

Where $C_{v(dense)}$ is the volume heat capacity of the dense ceramic and 0.29 J g^{-1} K^{-1}, as measured by differential scanning calorimetry (DSC). Fig. S4b shows that an increase of CNT content from 0 wt. % to 1.2 wt. % led to C_v decreasing slightly from 0.29 J g^{-1} K^{-1} to 0.27 J g^{-1} K^{-1}, which is favorable to the improvement of the $F_E^{'}$ figure of merit for pyroelectric energy harvesting (Equation 4); it is also advantageous for the sensing figures of merit (Equations 1-3). To understand the crystalline morphology of the porous PMN-PMS-PZT: 0.3CNT ceramic, transmission electron microscopy (TEM) was undertaken, as shown in Fig. 1b. The selected area electron diffraction (SAED) pattern shows clear diffraction rings that overlap on a broad diffused band, suggesting the formation of the polycrystalline structure of the ceramic; see Fig. 1c. In addition, the corresponding high-resolution transmission electron microscopy (HRTEM) image with the zone axis (110), revealing the lattice grain distance, which exhibits a good fit with the result from XRD refinement; see Fig. 1d and Fig. S5, respectively.

3.1.3 PFM measurement

To investigate the origin of the piezoelectricity, strain response and temperature-dependent piezoelectric properties, the domain structure, local piezoelectric response and polarization switching were studied by PFM. Both vertical PFM (V-PFM) and lateral PFM (L-PFM) images of PMN-PMS-PZT and PMN-PMS-PZT: 0.3CNT, measured at room temperature are presented in Figs. S6, 7 and Figs. 1e-g, respectively. These provide

vital information on the distribution of the out-of-plane component of the polarization of the materials. The amplitude images exhibited a clear contrast, and the differences of the phase angles were close to 180°, indicating the existence of different polarization directions. In addition, the domain regions with relatively smaller amplitude had different phases from those with higher amplitude since the internal bias field or alignment of defects during measurement process produced no, or small, piezoresponse in the upward or downward direction in the PFM mapping, which was induced by small tip bias [40].

To understand the local domain switching behavior, the out-plane of PFM phase and amplitude of dense PMN-PMS-PZT and porous PMN-PMS-PZT: 0.3CNT were investigated, as shown in Figs. 2a-f and Fig. S8, respectively. Both exhibited a 180° and non-180° contrast of domain orientation in the phase images, indicating an arbitrary domain distribution prior to the applied electric field. Fig. 2b shows that a bias of −20 V was sufficient to induce almost complete domain switching in PMN-PMS-PZT, which can be demonstrated by a complete 180° phase contrast between the 3 × 3 μm^2 and 1 × 1 μm^2 areas. In comparison, a bias of −50 V was able to induce a stronger domain switching (Fig. 2c). While for PMN-PMS-PZT: 0.3CNT, only a small portion of domain switching is induced with a bias of −20 V and no obvious change in the domain switching in the phase image with a bias of −50 V. However, there was more change in amplitude images (Figs. S8e, f). Such observations were further verified by the ambiguous contrast between the electrically poled 3 × 3 μm^2 and 1 × 1 μm^2 areas. These results demonstrate that domain switching in dense PMN-PMS-PZT is easier than that of porous PMN-PMS-PZT: 0.3CNT, which can be ascribed to the porosity in the latter microstructure, suggesting that the porosity can reduce to the degree of domain switching and domain mobility and, thus, lead to a reduced level of switching for a particular electric field.

To investigate the effect of domains on the piezoelectric and strain properties, the surfaces were further probed by a switching spectroscopy-PFM (SS-PFM) technique. Figs. S9 a-d and e-h show the local butterfly piezoresponse loops of dense PMN-PMS-PZT and porous PMN-PMS-PZT: 0.3CNT, respectively, at various tip bias voltages. Both samples showed an increased in the amplitudes with an increase of the tip voltage. In addition, the dense PMN-PMS-PZT showed a larger amplitude compared to the porous PMN-PMS-PZT: 0.3CNT suggesting that the introduction of porosity reduced the amplitude to the reduced fraction of piezoelectric material and the potential of pinning of domain walls due to the presence of porosity [41]. To better understand the local piezoresponse, microscopic piezoresponse hysteresis loops, which were derived

from the butterfly loop by anti-folding the region under the −40 V to 0 V data are presented in Fig. 2g; where R_S^+ and R_S^- are the forward and reverse saturation response, respectively, while R_0^+ and R_0^- are the forward and reverse remnant response, respectively. The local maximum piezoresponse, $D_{s,max}$, and remnant piezoresponse, D_{rem}, are defined as $D_{\mathrm{smax}} = (R_{\mathrm{s}}^+ - R_{\mathrm{s}}^-)/2$ and $D_{rem} = (R_0^+ - R_0^-)/2$, respectively [42]. Figs. 2h and i show that the dense PMN-PMS-PZT ceramics had a higher $D_{s,max}$ and D_{rem} than the porous PMN-PMS-PZT: 0.3CNT under similar tip bias voltages, confirming that the pores and defects at grains can limit domain reversal and weaken the local piezoresponse under an electric field. Intuitively, this actively demonstrates that the changes in micro-domains can affect the macroscopic piezoelectric and strain properties. Khachaturyan *et al.* [43] examined porosity in lead zirconate titanate ceramics, where it was thought that residual carbon in pores may provide local screening of the applied electric field, which can restrict domain switching, while the pore surface morphology can also impact on domain morphology and pinning. In contrast, the presence of pores could provide stress relief could facilitate domain switching. An additional factor is a contrast in the electric field distribution around a pore, where it has been shown that the applied electric field is greatest in the low permittivity pore phase and correspondingly reduced within the ferroelectric phase; thereby reducing domain mobility at the particular applied electric field [44].

To understand the effect of microscopic temperature stability of domain on the macroscopic temperature stability of electrical properties, the V-PFM amplitudes of PMN-PMS-PZT and PMN-PMS-PZT: 0.3CNT from 25 to 100 °C are presented in Figs. S10a-d and 3a-d, respectively. Typical butterfly loops of PMN-PMS-PZT and PMN-PMS-PZT: 0.3CNT from 25 to 100 °C are shown in Figs. S10 e-h and 3e-h. All domains demonstrated 180° phase switching under the tip bias voltages, indicating a typical ferroelectric-like piezoelectric response. The local hysteresis loops are shown in Figs. 3i and S10i, respectively. The related parameters of two samples are defined in Figs. 3j and S10j, respectively. For dense PMN-PMS-PZT ceramic, the amplitude increased initially and then decreased with increasing temperature, while for porous PMN-PMS-PZT: 0.3CNT sample, the amplitude of piezoresponse increased with increasing temperature, which can be explained that the electroelastic field generated by the tip decreases due to the extrinsic contribution - where a new nucleus is formed and domains grow, resulting in a greater degree of domain switching in the crystal and an increased piezoresponse [40]. As a result, the microscopic piezoelectric parameters, D_{smax} and D_{rmax} of both samples increased initially with an increase in temperature. With a further increase in temperature, the

amplitude of piezoresponse of the dense PMN-PMS-PZT sample decreased, while that of the porous sample continued to increase, see Fig. S10k and 3k. This may be due to the fact that for the dense PMN-PMS-PZT sample, with a further increase the temperature, there is a stronger coupling between the grain boundaries and the domain walls that constrains domain wall motion, resulting in a decrease of the piezoresponse [42]. When a high temperature is applied on to the materials, structural changes or redistribution of impurities can occur, causing the depinning of domains that were previously restricted, thereby increasing the piezoresponse [40].

These changes in the domain structure can also contribute to the switching kinetics. The coercive field of the dense PMN-PMS-PZT sample exhibited a similar variation; increasing first with increasing temperature and then decreasing with increasing temperature, with D_{smax} and D_{rmax}, see Fig. S10l. Initially, the coercive field increased which can be ascribed to the internal bias field [40, 42]. Subsequently, it decreased due to weaker internal bias field and more mobile domains with increasing temperature. While for porous PMN-PMS-PZT ceramic, with increasing temperature, the depinning of domains is reduced and domains are increasingly more mobile with increasing temperature, and consequently the coercive field is decreased, see Fig. 3l.

3.2 Electrical properties and figure of merits of porous ceramics PMN-PMS-PZT: *x*CNT

3.2.1 Dielectric, ferroelectric and pyroelectric properties

Figs. 4a, b show the dielectric constant and loss tangent with the temperature variations from 25 °C to 300 °C at 1 kHz, respectively. As can be seen from Fig. 4a, the relative permittivity (ε_r) at the corresponding Curie temperature (T_c) decreases with increasing porosity, in particular at 32 °C from $\varepsilon_r \sim 252$ to $\varepsilon_r \sim 210$, as seen in the inset. In addition, the Curie temperature for the PMN-PMS-PZT material with the addition of x = 0, 0.3, 0.6, 0.9 and 1.2 wt.% CNT are 217, 217.9, 219, 219.9 and 221°C, respectively, suggesting it gradually shifts to higher temperature with increasing porosity. This is due to the introduction of pores which (i) has a lower dielectric constant than PMN-PMS-PZT, and (ii) reduces the internal stress in the porous material [38], leading to the decrease of ε_r and an increase of T_c. According to the figures of merit, Equations (1) to (4), the decrease in ε_r increases its the pyroelectric energy harvesting performance. Similarly, the loss tangent increased with increasing CNT content, see inset of Fig. 4b, which is mainly due to the introduction of pores with high dielectric loss in porous ceramics [40].

The polarization-electric field (P-E) hysteresis loops of the PMN-PMS-PZT: *x*CNT samples at room

temperature are presented in Fig. 4c. All samples exhibited the typical ferroelectric property and the saturation polarization (P_s) gradually decreased from 55.98 μC cm^{-2} to 18.53 μC cm^{-2} when the CNT content increased from 0 to 1.2 wt.%, which is due to the increasing porosity and reduction on fraction of active material and the additional depolarization field to the presence of pores. Similarly, the remnant polarization, P_r, exhibited the same change (see Fig. S11) with P_s decreasing with increasing CNT content due to the increase in porosity in the PMN-PMS-PZT matrix, leading to a reduced amount domain of active material and the additional depolarization due the electric field distribution around the pore [45] and, thus, P_r decreased under the same electric field.

In addition, the coercive field E_c initially decreased with increasing CNT content and then increased, see Fig. S11, which can be explained that when CNT content is lower than 0.9 wt.%, the presence of a relatively small fraction on pores in the ceramic have no obvious effect on the electric field distribution and lowers the stiffness of the matrix to facilitate domains motion, to decrease E_c [45]. With a further increase in CNT content, the fraction of pores increased to a level which affected the electric field distribution due to the permittivity contrast between the low permittivity pores and high permittivity ferroelectric, thereby leading to reduced switching of ferroelectric domains; thus, E_c increased sharply when the CNT content was 1.2 wt.%. From Fig. 4d, the pyroelectric properties from room temperature to 50 °C demonstrated a similar decreasing trend where the P_s and the maximum value of the pyroelectric coefficient is gradually shifted to a lower temperature with increasing CNT content; this can be attributed to the faster pyroelectric response of the ceramic with increasing porosity under the same temperature field [38].

3.2.2 Figure of merits

In order to compare the FOMs (Equations 1 to 4) of all samples, the ε_r and the pyroelectric coefficients decreased from 4331 μC m^{-2} K^{-1} to 1711 μC m^{-2} K^{-1} (Fig. 4e) at 32 °C. Thus, we can calculate the corresponding responsivity for a sensor at 32 °C as shown in Figs. 4f-h and Fig. S12, respectively. It can be seen that F_I remained relatively constant with CNT content (up to 0.6 wt.%) and decreased with increasing CNT content (0.6 – 1.2 wt.%), while F_V and $F_E^{'}$ had an initial increase with increasing CNT content (up to 0.6 wt.%) and then decreased. For PMN-PMS-PZT: 0.6CNT the highest F_v and $F_E^{'}$ is 0.92 m^2 C^{-1} and 1.71 nm^3 J^{-1}, respectively. This indicates that porous structure can enhance the voltage responsivity for sensing F_V and energy harvesting figure of merit $F_E^{'}$.

3.3 Thermal energy harvesting of the porous ceramics PMN-PMS-PZT: *x*CNT

Fig. 5 shows the charge generation process of pyroelectric energy harvesting. A charging process takes place under short-circuit conditions when the pyroelectric material serves as the dielectric material and is sandwiched between two plates of a capacitor. Initially, the electric dipoles oscillate randomly in the material and reach an equilibrium state at a constant room temperature (dT/dt =0). No current is generated in the external circuit since the temperature and spontaneous polarization is constant (Fig. 5a). With an increase in temperature across the capacitor ($dT/dt > 0$), the electric dipoles oscillate within a larger degree of alignment, resulting in a decrease in polarization and the generation of a current in the external circuit (Fig. 5b). In addition, if the temperature is reduced ($dT/dt < 0$), the dipoles become realigned leading to an increase in polarization and a reverse current flow in the external circuit (Fig. 5c). Figs. 5d-j demonstrate the pyroelectric energy harvesting performance of the dense PMN-PMS-PZT devices with a diameter 9 mm and thickness 0.28 mm of ceramic pellets (see Fig. S13) under the cyclic temperatures from 25 to 50 °C (Fig. 5d). In the forward connection, the output voltage and dT/dt for all devices are shown in Figs. 5e-j. The output voltage and power are shown in Fig. S14a and the corresponding parameters are summarized in Table S1. In a reversed connection, the corresponding signals were inverted with the identical value with that in forward connection as shown in Fig. S14b-f. It can be seen that the output voltage, current and power of the devices peaked when the CNT content is 0.3 wt.%. Specifically, when the CNT content increased from 0 to 0.3 wt.%, the output peak voltage increased from 7.6 V to 13.3 V, leading to an increase of 75.4%. Subsequently, the output voltage for the samples with high CNT contents exhibited a gradually decreasing in voltage (0.6 wt.%, 0.9 wt.% and 1.2 wt.% had a peak voltage of 11.13, 9.51 and 8.69 V, respectively). Correspondingly, the output power increased from 5.77 to 17.78 μW when the CNT content increased from 0 to 0.3 wt.%, leading to an increase of 208%, and then decreased with a further increase in CNT content. Compared with the pristine dense ceramic, the output power for the samples with 0.6 wt.%, 0.9 wt.% and 1.2 wt.% CNT continued to exhibit an improvement of 114.5%, 56.7% and 30.8%, respectively. It can be seen that the porous ceramic formed using the CNT can effectively improve the performance of pyroelectric energy harvesters, which provides the potential application of the next wearable sensing devices and wireless sensor network nodes.

4. Conclusion

Porous pyroelectric ceramics with embedded carbon nanotubes (CNT) were carefully designed to achieve

high-performance thermal to electrical energy conversion. It was observed that porosity and defects in grains can restrict domain reversal and weaken the local piezoresponse under an applied electric field, which was validated via detailed micro-scale dipole switching observed by piezo force microscopy. The V-PFM amplitudes of PMN-PMS-PZT and PMN-PMS-PZT: 0.3CNT from 25 to 100 °C indicated a typical ferroelectric-like piezoelectric response, which is ascribed to the impact of porosity and temperature on the domain mobility. Compared with the pristine dense PMN-PMS-PZT, porous PMN-PMS-PZT exhibited an enhanced figure of merits including voltage responsibility and energy harvesting figure of merit due to lower permittivity and heat capacity as a result of the introduction of porosity. Among all the composition studied, PMN-PMS-PZT: 0.3CNT showed the highest power output of 17.78 μW which was an increase of 208% compared to the pristine PMN-PMS-PNT. This work represents an advancement in the community of thermal energy conversion via materials engineering and innovation.

CRediT authorship contribution statement

Qingping Wang: Methodology, Data curation, Writing – original draft. **Shihua He:** Methodology, Data curation. **Chris R Bowen:** Supervision, Methodology, Data curation, Writing – review & editing. **Xiao Xiao:** Methodology, Data curation. **Jin An Sam Oh:** Methodology, Writing – review & editing. **Jianguo Sun:** Methodology, Data curation. **Kaiyang Zeng:** Methodology, Data curation. **Wen Lei:** Methodology, Data curation. **Jun Chen:** Supervision, Writing – review & editing.

Declaration of Competing Interest

The authors declare that they have no known competing financial interests or personal relationships that could have appeared to influence the work reported in this paper.

Acknowledgments

Q. Wang acknowledges the National Natural Science Foundation of China (Grant No. 51902094), Guidance Project on Scientific Research Program of Hubei Province Education (Grant No. B2015014) and Postdoctoral Scholarship from China Scholarship Council (Grant No. 201908420009). J. Chen acknowledges the Henry Samueli School of Engineering & Applied Science and the Department of Bioengineering at the University of California, Los Angeles for the startup support.

References

[1] C. R. Bowen, J. Taylor, E. LeBoulbar, D. Zabek, A. Chauhanc, R. Vaishet, Pyroelectric materials and devices for energy harvesting applications, Energy Environ. Sci. 7 (2014) 3836-3856.

[2] Y. Fang, G. Chen, M. Bick, J. Chen, Smart textiles for personalized thermoregulation. Chem. Soc. Rev. 50 (2021) 9357-9374.

[3] Y. Zhou, X. Zhang, J. Xu, Y. Fang, G. Chen, Y. Song, S. Li, J. Chen, Giant magnetoelastic effect in soft systems for bioelectronics, Nat. Mater. 20 (2021) 1670-1676.

[4] G. Chen, X. Xiao, X. Zhao, T. Tat, M. Bick, J. Chen, Electronic textiles for wearable point-of-care systems, Chem. Rev. 122 (2022) 3259-3291.

[5] G. Chen, Y. Li, M. Bick, J. Chen, Smart textiles for electricity generation, Chem. Rev. 120 (2020) 3668-3720.

[6] X. Zhao, H. Askari, J. Chen, Nanogenerators for smart cities in the era of 5G and Internet of Things, Joule 16 (2021) 1391-1431.

[7] X. Zhao, Y. Zhou, J. Xu, G. Chen, Y. Fang, T. Tat, X. Xiao, Y. Song, S. Li, J. Chen, Soft fibers with magnetoelasticity for wearable electronics, Nat. Commun. 12 (2021) 6755.

[8] G. Chen, X. Zhao, S. Andalib, J. Xu, Y. Zhou, T. Tat, K. Lin, J. Chen, Discovering giant magnetoelasticity in soft matter for electronic textiles, Matter. 4 (2021) 3725-3740.

[9] H. Ryu, H. J. Yoon, and S. W. Kim, Hybrid energy harvesters: toward sustainable energy harvesting, Adv. Mater. 31 (2019) 1802898.

[10] L. Jin, X. Xiao, W. Deng, A. Nashalian, D. He, V. Raveendran, C. Yan, H. Su, X. Chu, T. Yang, W. Li, W. Yang, J. Chen, Manipulating relative permittivity for high-performance wearable triboelectric nanogenerators, Nano. Lett. 20 (2020) 6404-6411.

[11] A. Libanori, G. Chen, X. Zhao, Y. Zhou, J. Chen, Smart textiles for personalized healthcare, Nat. Electron. 5 (2022), 142-156.

[12] C. R. Bowen, J. Taylor, E. Le Boulbar, D. Zabek, V. Y. Topolov, A modified figure of merit for pyroelectric energy harvesting, Mater. Lett. 138 (2015) 243-246.

[13] C. R. Bowen, H. A. Kim, P. M. Weaver, S. Dunn, Piezoelectric and ferroelectric materials and structures for energy harvesting applications, Energy. Environ. Sci. 7 (2014) 25-44.

[14] J. W. Stewart, J. H. Vella, W. Li, S. Fan, M. H. Mikkelsen, Ultrafast pyroelectric photodetection with on-chip spectral filters, Nat. Mater. 19 (2020) 158-162.

[15] Y. Zhang, M. Xie, J. Roscow, Y. Bao, K. Zhou, D. Zhang, C. R. Bowen, Enhanced pyroelectric and piezoelectric properties of PZT with aligned porosity for energy harvesting applications, J. Mater. Chem. A 5 (2017) 6569-6580.

[16] Q. Wang, X. Zhang, C. R. Bowen, M. Li, J. Ma, S. Qiu, H. Liu, S. Jiang, Effect of Zr/Ti ratio on microstructure and electrical properties of pyroelectric ceramics for energy harvesting applications, J. Alloys. Compd. 710 (2017) 869-874.

[17] A. Hussain, N. Sinha, S. Bhandari, H. Yadav, B. Kumar, Synthesis of $0.64Pb(Mg_{1/3}Nb_{2/3})O_3$-$0.36PbTiO_3$ ceramic near morphotropic phase boundary for high performance piezoelectric, ferroelectric and pyroelectric applications, J. Asian. Ceram. Soc. 4 (2016) 337-343.

[18] M.Wojtaś, D.V.Karpinsky, M.V.Silibin, S.A.Gavrilov, A.V.Sysa, K.N.Nekludov, S.V.Dubkov, Pyroelectricity in graphene oxide doped P(VDF-TrFE) films. Polym. Test. 71 (2018) 296-300.

[19] A. Siao, C. K. Chao. C. C. Hsiao, Study on pyroelectric harvesters with various geometry, Sensors 15 (2015) 19633-19648.

[20] A. Siao, C. K. Chao, C .C. Hsiao, A strip cell in pyroelectric devices, Sensors (Basel) 16 (2016) 375.

[21] M.Wojtas, D.V.Karpinsky, M.V.Silibin, S.A.Gavrilov, A.V.Sysa, K.N.Nekludov, Dielectric properties of graphene oxide doped P(VDF-TrFE) films. Polym. Test. 60 (2017) 326-332.

[22] S. Jiang, P. Liu, X. Zhang, L. Zhang, Q. Li, J. Yao, Y. Zeng, Q. Wang, G. Zhang, Enhanced pyroelectric properties of porous $Ba_{0.67}Sr_{0.33}TiO_3$ ceramics fabricated with carbon nanotubes, J. Alloys. Compd. 636 (2015) 93-96.

[23] L. Han, S. Guo, S. Yan, F. Cao, W. Guo, C. Yao, X. Dong, G. Wang, Enhanced pyroelectric properties of $Pb_{0.3}Ca_{0.15}Sr_{0.55}TiO_3$ ceramic with first-order dominated phase transition under low bias field, Appl. Phys. Lett. 110 (2017) 102905.

[24] K. S. Srikanth, V. P. Singh., R. Vaish, Pyroelectric performance of porous $Ba_{0.85}Sr_{0.15}TiO_3$ ceramics, Int. J. Appl. Ceram. Technol. **15**, 140-147 (2018).

[25] J. Wu, W. Miao, Z. Wu, X. Xu, H. You, A'X. Xue, Y. Jia, Strong pyro-catalysis of pyroelectric $BiFeO_3$ nanoparticles under a room-temperature cold-hot alternation, Nanoscale 8 (2016) 7343-7350.
[26] T. Zhao, W. Jiang, D. Niu, H. Liu, B. Chen, Y. Shi, L. Yin, B. Lu, Flexible pyroelectric device for scavenging thermal energy from chemical process and as self-powered temperature monitor, Appl. Energy 195 (2017) 754-760.
[27] X. Wang, Y. Dai, R. Liu, X. He, S. Li, Z. L. Wang, Light-triggered pyroelectric nanogenerator based on a pn-Junction for self-powered near-Infrared photosensing, ACS Nano 11 (2017) 8339-8345.
[28] K. Chen, X. Gai, G. Zhou, Y. Shan, C. Zhao, K. Shen, Z. Fan, Study on a new type of pyroelectric materials with structure of tourmaline, Ceram. Int. 45 (2019) 10684-10690.
[29] J. Roscow, Y. Zhang, J. Taylor, C. R. Bowen, Porous ferroelectrics for energy harvesting applications, Eur. Phys. J. Spec. Top. 224 (2015) 2949-2966.
[30] K. S. Srikanth, V. P. Singh, R. Vaish, Enhanced pyroelectric figure of merits of porous $BaSn_{0.05}Ti_{0.95}O_3$ ceramics, J. Eur. Ceram. Soc. 37 (2017) 3943-3950.
[31] H. Kara, R. Ramesh, R. Stevens, C. R. Bowen, Porous PZT ceramics for receiving transducers, IEEE Trans. Ultrason. Ferroelectr. Freq. Control. 50 (2003) 289-296.
[32] J. Yang, J. Yu, Y. Huang, Recent developments in gelcasting of ceramics, J. Eur. Ceram. Soc. 31 (2011) 2569-2591.
[33] C. Minas, D.Carnelli, E. Tervoort, A. R. Studart, 3D printing of emulsions and foams into hierarchical porous ceramics. Adv. Mater. 28 (2016) 9993-9999.
[34] H.T. Naeem, The influence of different pore forming agents on piezoelectric and dielectric properties of porous PZT-PCN ceramics, Materials Today: Proceedings 20 (2020) 531-534.
[35] F. Abdullah, A. Nemati, R. Bagheri, Synthesis and characterization of porous PZT-PCN ceramics, J. Ceram. Process. Res. 16 (2015) 572-577.
[36] E. D. Deivarajan, T. Deivarajan, A concise review encircling lead free porous piezoelectric ceramics, Acta Phys. Pol. A 136 (2019) 555-565.
[37] Q. Wang, C. R. Bowen, W. Lei, H. Zhang, B. Xie, S. Qiu, M.Li, S. Jiang, Improved heat transfer for pyroelectric energy harvesting applications using a thermal conductive network of aluminum nitride in PMN-PMS-PZT ceramics, J. Mater. Chem. A 6 (2018) 5040-5051.
[38] Q. Wang, C. R. Bowen, R. Lewis, J. Chen, W. Lei, H. Zhang, M. Li, S. Jiang, Hexagonal boron nitride nanosheets doped pyroelectric ceramic composite for high-performance thermal energy harvesting, Nano Energy 60 (2019) 144-152.
[39] K. S. Srikanth, V. P. Singh, R. Vaish, Enhanced pyroelectric figure of merits of porous $BaSn_{0.05}Ti_{0.95}O_3$ ceramics, J. Eur. Ceram. Soc. 37 (2017) 3943-3950.
[40] J. Luo, W. Sun, Z. Zhou, Y. Bai, Z. Wang, G. Tian, D. Chen, X. Gao, F. Zhu, J. F. Li, Domain evolution and piezoelectric response across thermotropic phase boundary in $(K,Na)NbO_3$ -based epitaxial thin films, ACS Appl. Mater. Interfaces 9 (2017) 13315-13322.
[41] C. Xie, H. Zhao, L. Du, H. Du, P. Wu, Enhanced ferroelectricity for nanoporous barium titanate: a phase-field prediction, Philos. Mag. Lett. 101 (2021) 341-352.
[42] Z. Liu, C. Zhao, J. Li, K. Wang, J. Wu, Large strain and temperature-insensitive piezoelectric effect in high-temperature piezoelectric ceramics, J. Mater. Chem. C 6 (2018) 456-463.
[43] R. Khachaturyan, S. Zhukov, J. Schultheiß, C. Galassi, C. Reimuth, J. Koruza, H. Seggern, Y. A. Genenko, Polarization-switching dynamics in bulk ferroelectrics with isometric and oriented anisometric pores, J. Phys. D: Appl. Phys. 50 (2017) 045303.
[44] G. Martínez-Ayuso, M. I. Friswell, H. H. Khodaparast, J. Roscow, C. R. Bowen, Electric field distribution in porous piezoelectric materials during polarization, Acta. Mater. 173 (2019) 332-341.
[45] Y. Zhang, J. Roscow, R. Lewis, H. Khanbareh, V. Y. Topolov, M. Xie, C.R. Bowen, Understanding the effect of porosity on the polarisation-field response of ferroelectric materials, Acta. Mater. 154 (2018) 100-112.

Figures and Captions

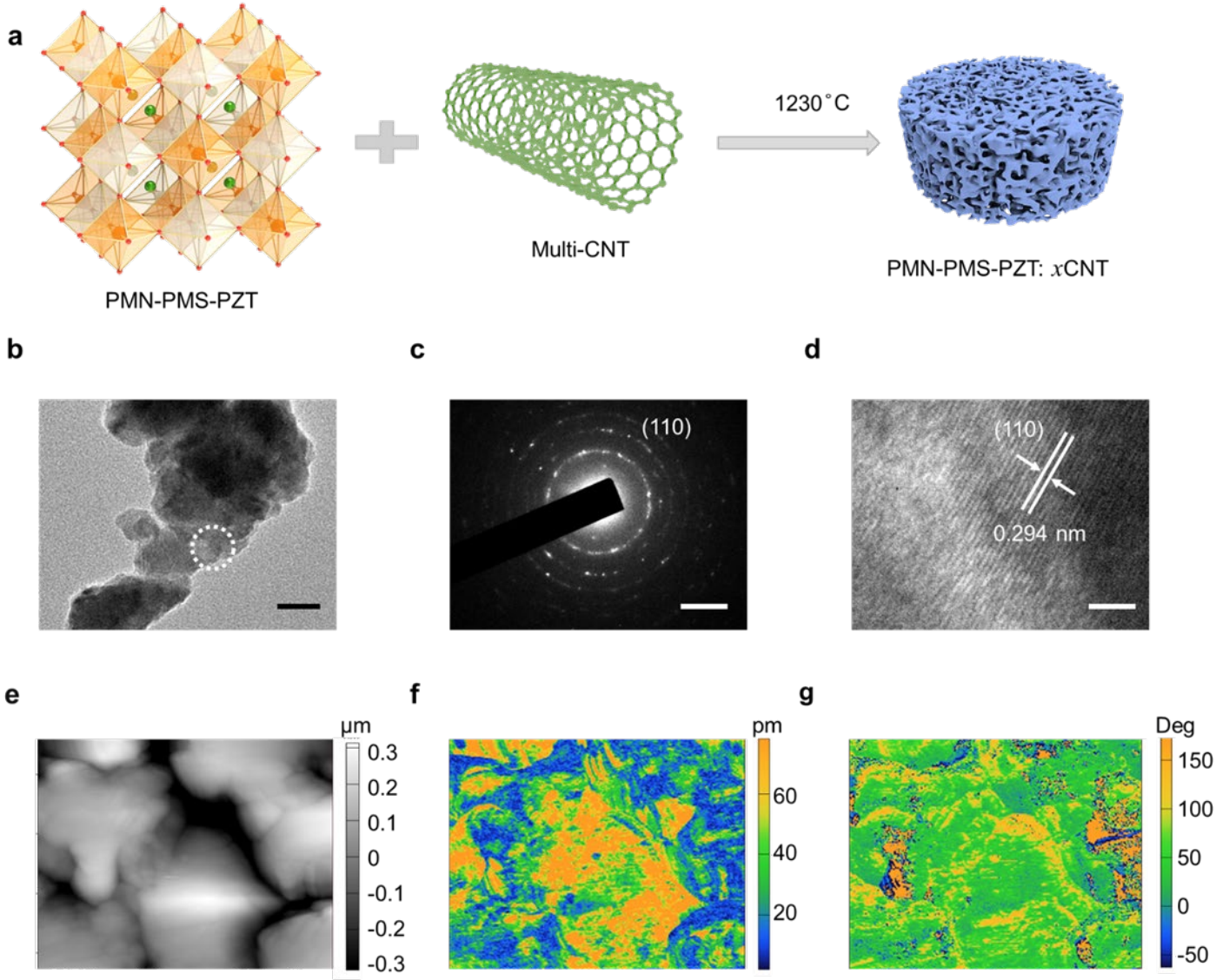

Fig. 1. Morphology and PFM properties. (a) Schematic of synthesis process of porous PMN-PMS-PZT: *x*CNT (*x*=0.3, 0.6, 0.9, 1.2), (b) TEM micrograph, (c) SAED pattern, (d) HRTEM image, and Vertical Piezoresponse Force Microscopy (V-PFM) images of (e) Surface image (f) amplitude and (g) phase of PMN-PMS-PZT: 0.3CNTceramic.

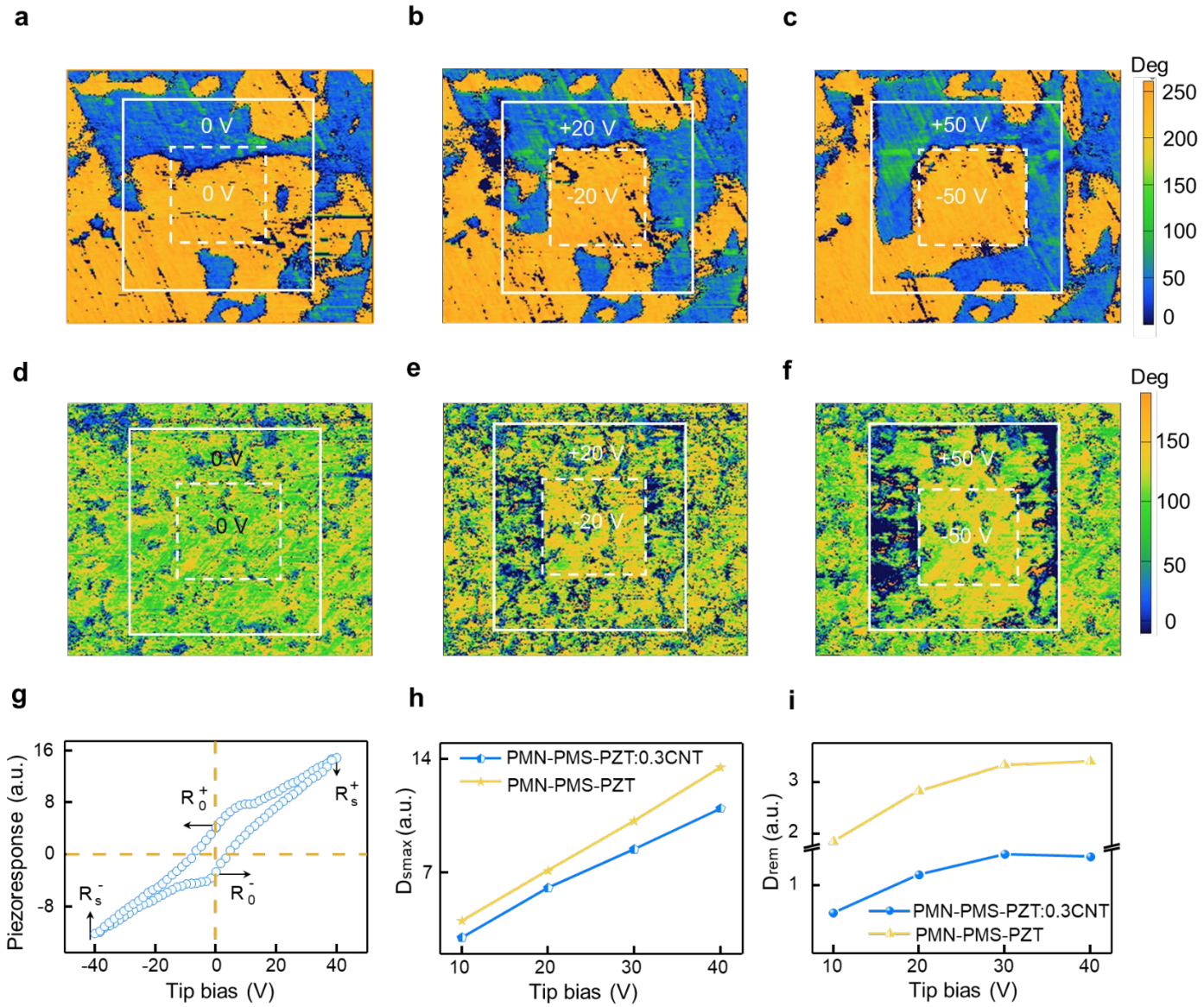

Fig. 2. PFM properties of the PMN-PMS-PZT: 0.3CNT sample at different voltages. PFM phase images of (a)-(c) PMN-PMS-PZT and (d)-(f) PMN-PMS-PZT: 0.3CNT ceramics before and after poling with ± 20 and ± 50 V. Note that the 3 × 3 μm^2 area (denoted by the larger solid box) indicates upward switching of domains with a scanning voltage of +20 or +50 V while the internal 1 × 1 μm^2 area (denoted by the smaller dashed box) represents inverse downward switching of domains when subjected to a voltage of −20 or −50 V. (g) Piezoresponse hysteresis loop, (h) $D_{s,max}$ and (i) D_{rem} of PMN-PMS-PZT and PMN-PMS-PZT: 0.3CNT.

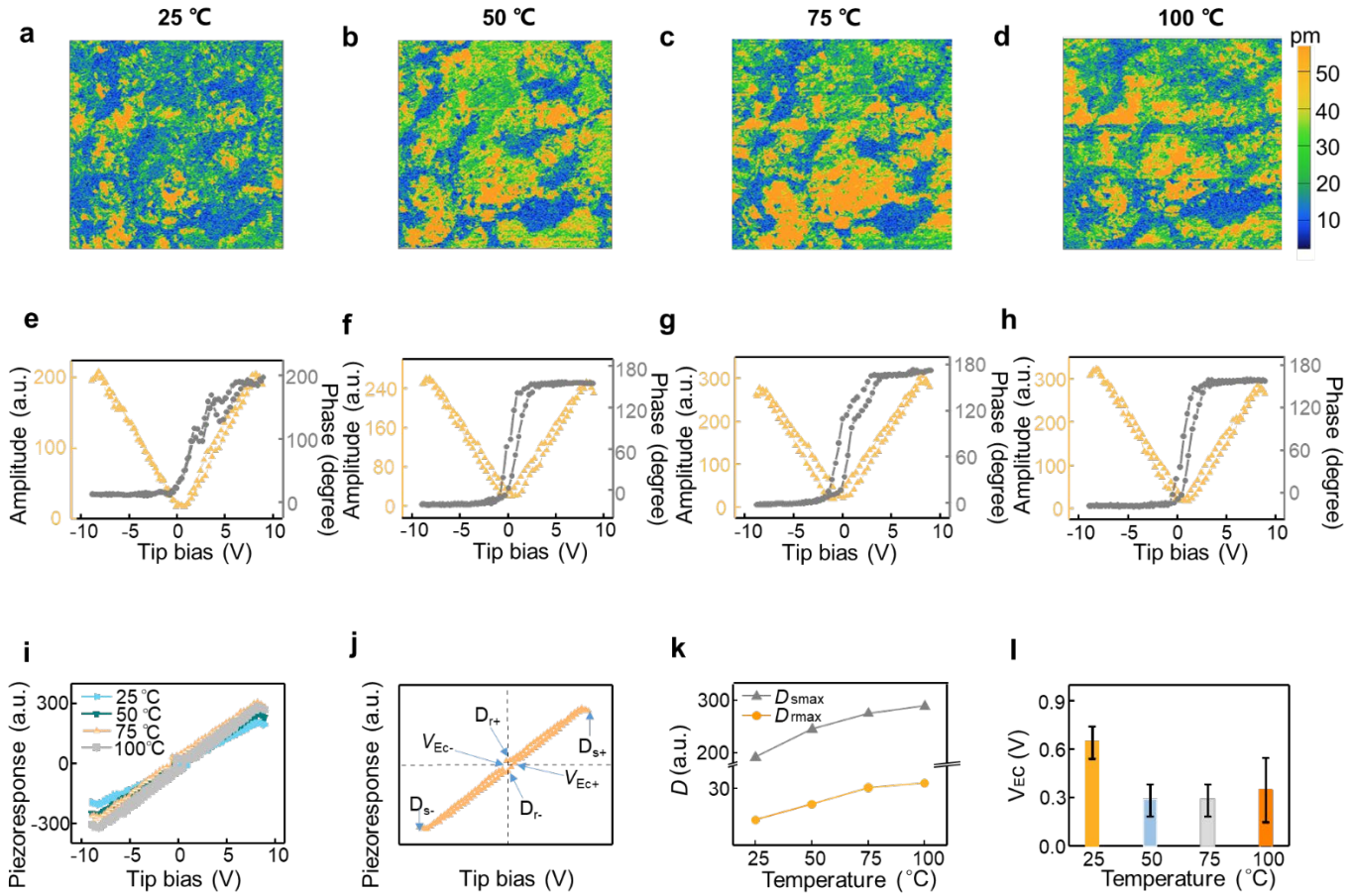

Figs. 3. PFM properties of the PMN-PMS-PZT: 0.3CNT sample at different temperatures. (a)-(d) PMN-PMS-PZT: 0.3CNT sample at different temperatures. (e)-(h) Typical butterfly loops of PMN-PMS-PZT: 0.3CNT sample, measured at various temperatures. (i) VPFM hysteresis loops at different temperatures. (j) Piezoresponse hysteresis loop: forward coercive voltage V_{Ec+} and reverse coercive voltage V_{Ec-}, forward saturation response D_{S+} and reverse saturation response D_{S-}, forward remnant response D_{r+} and reverse remnant response D_{r-}. (k) D_{smax} and D_{rmax} at different temperatures. (l) Coercive voltage with different temperatures.

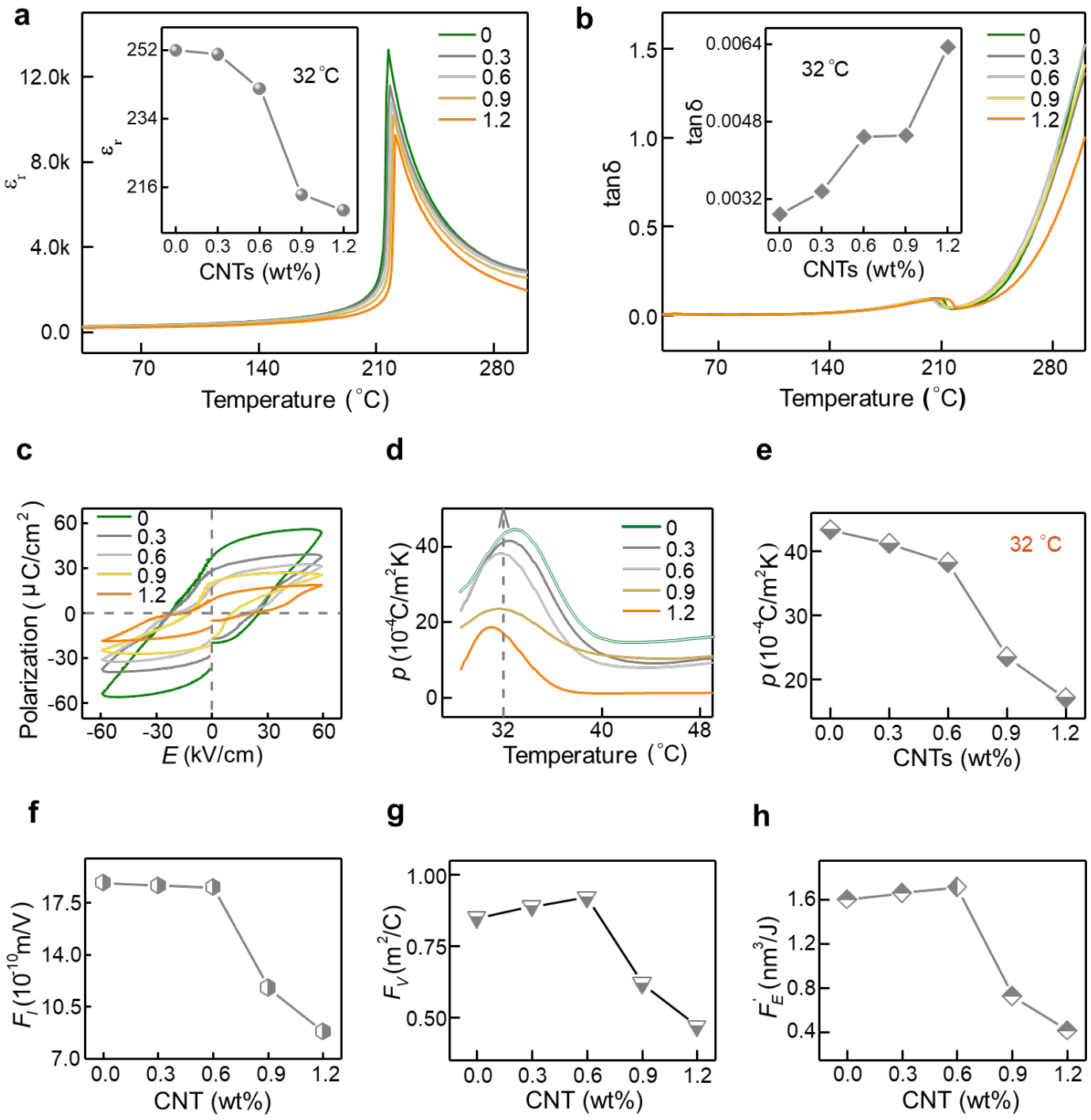

Fig. 4. Electrical properties and figure of merits of PMN-PMS-PZT: *x*CNT (*x* = 0, 0.3, 0.6, 0.9, 1.2) samples. (a) Dielectric constant and (b) dielectric loss with temperatures from room temperature to 300 °C, (c) *P*-*E* loops, Pyroelectric coefficient with (d) temperature from 25 to 50 °C, and (e) various CNT content at 32 °C. (f)-(h) Figure of merits of sensing (F_I, F_V) and energy harvesting (F'_E) with various CNT content at 32 °C.

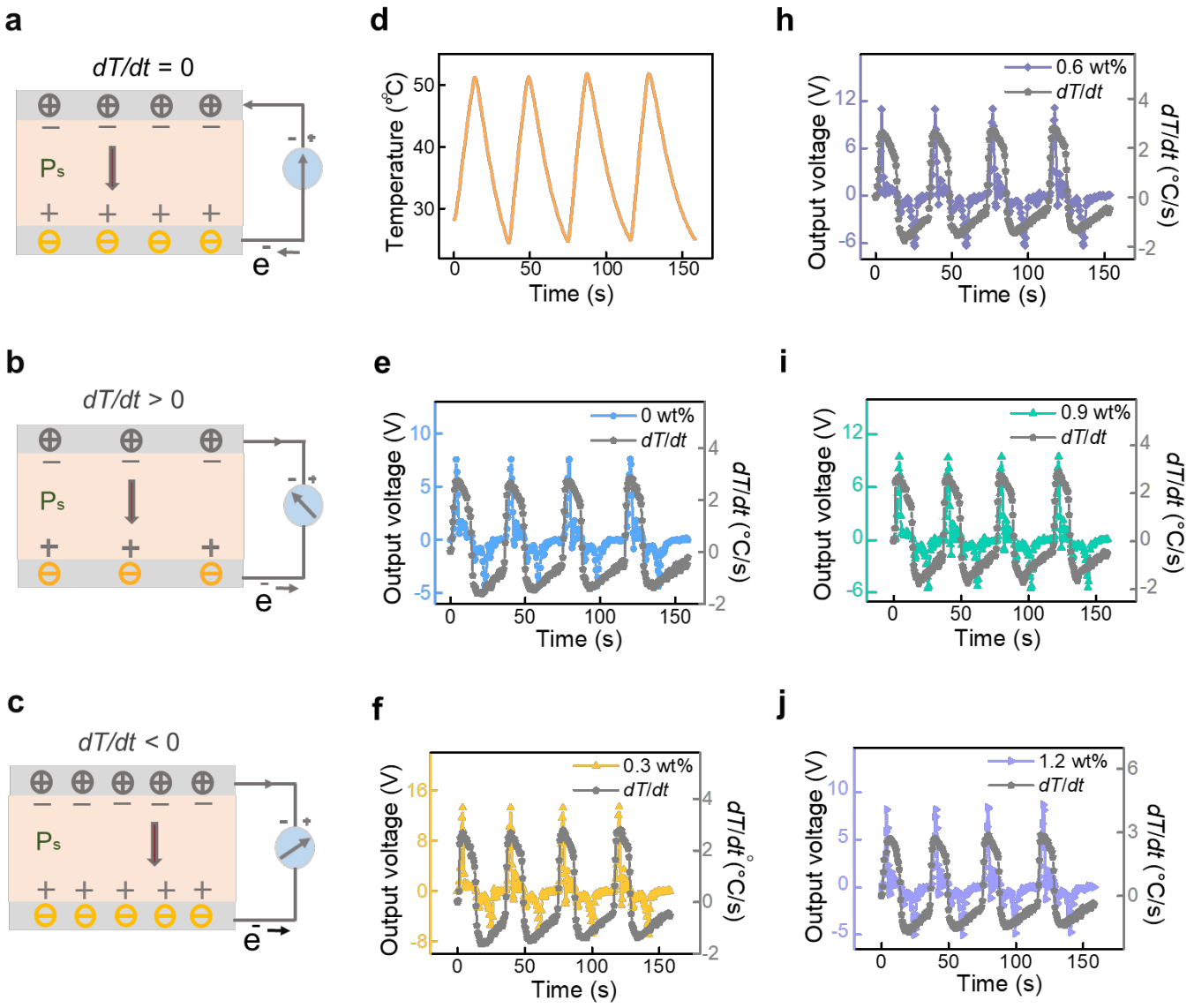

Fig. 5. Thermal energy harvesting of PMN-PMS-PZT: *x*CNT (x = 0, 0.3, 0.6, 0.9, 1.2) samples. (a)-(c) Mechanism of the pyroelectric effect, (d) Cyclic temperature, and (h)-(j) output voltage and the rate of temperature change in forward connection.

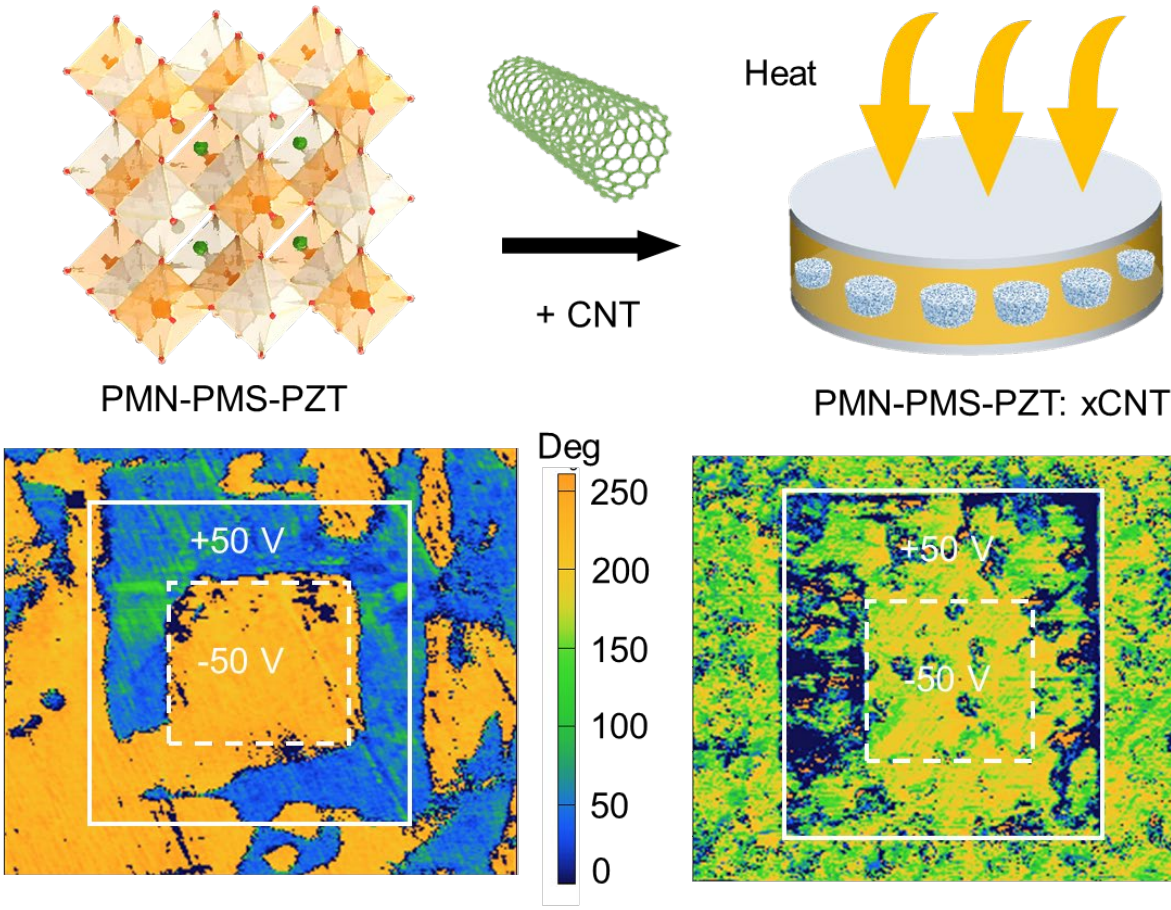
Heat
+ CNT
PMN-PMS-PZT
PMN-PMS-PZT: xCNT
Deg
250
200
150
100
50
0
+50 V
-50 V
Deg
150
100
50
0
+50 V
-50 V

TOC